# SUPPLEMENTARY METHODS

## A. Detailed implementation of the baseline method

Here, we describe the Rytov-based baseline method used for comparison, which includes both orientation estimation and 3D reconstruction[1–3]. In microfluidic channels, the flow is laminar, so cells travel along approximately straight trajectories. The cross-sectional velocity profile is parabolic, so a cell located off-center experiences differential viscous forces on opposite sides, inducing continuous rotation as it moves. In the commonly encountered stable flow regime, the cell rotates at an approximately constant angular velocity, so that the rotation angle is proportional to the distance traveled along the flow direction. Let $y_i$ denote the distance traveled by the cell from its initial position at the *i*-th image, and let *Y* be the distance corresponding to one full rotation. Assuming the initial position corresponds to a rotation angle of 0, the rotation angle $\theta_i$ is given by

$$\theta_i = \frac{2\pi\, y_i}{Y}.$$

Thus, the rotation angle increases linearly with the displacement from the starting point. Since the distance *Y* corresponding to one full rotation is initially unknown, it must be determined from the observed rotational motion. To this end, we define a coordinate system where the cell's rotation axis is aligned with the *x*-axis, the flow direction with the *y*-axis, and the incident light propagates along the *z*-axis. The cell is conceptually divided into ``upper'' and ``lower'' parts by the *y*-*z* plane (Fig. S1). Let $P_1$ and $P_2$ denote the geometric centroids of the upper and lower parts of the cell, respectively, computed from the binary mask in each observed image.

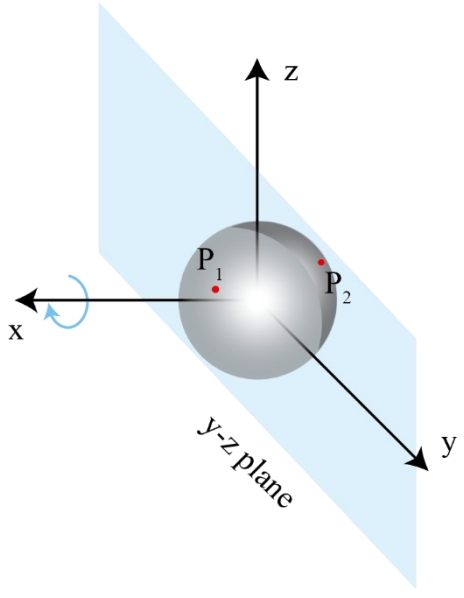


**Figure S1: Schematic illustration of a rolling cell in microfluidic flow.** For the baseline method, a coordinate system is defined where the cell's rotation axis is aligned with the *x*-axis, the flow direction with the *y*-axis, and the incident light propagates along the *z*-axis. The cell is conceptually divided into “upper” and “lower” parts by the *y*-*z* plane (Fig. S1). Let $P_1$ and $P_2$ denote the geometric centroids of the upper and

lower parts of the cell, respectively, computed from the binary mask in each observed image.

The orientation of the cell is characterized by the direction angle $\phi_i$, defined as the angle between the vector $\overrightarrow{P_1P_2}$ and the *x*-axis. During rolling, $\phi_i$ and $\theta_i$ can be approximated by a sinusoidal relationship of the form

$$\sin\phi_i = \frac{y_2 - y_1}{r_2 + r_1} = \frac{a_2 + a_1}{r_2 + r_1}\cos\theta_i,$$

So that

$$\phi_i = \arcsin\left(\frac{a_2 + a_1}{r_2 + r_1}\cos\left(\frac{2\pi y_i}{Y}\right)\right).$$

Here, $a_1$ and $a_2$ denote shape-dependent scaling factors, and $r_1$, $r_2$ are radial distances from the cell center to its hemispherical boundaries (Fig. S2). As the cell rotates at a constant angular velocity, $\phi_i$ varies sinusoidally with the displacement $y_i$. By fitting the observed $\phi_i$ versus $y_i$ $ data to a sinusoidal model, we can extract the period of rotation, which corresponds to the distance *Y* for one full cycle.

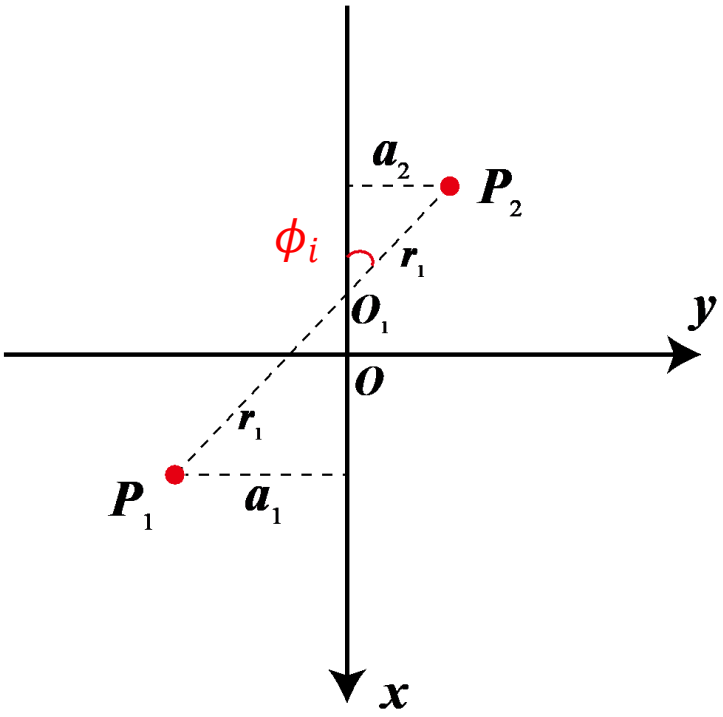


**Figure S2.** The positions of the centroids $P_1$ and $P_2$ are projected onto the x-y plane. Here, $r_1$ and $r_2$ denote the radial distances from the cell center (O) to the hemispherical boundaries, while $a_1$ and $a_2$ represent the displacements of $P_1$ and $P_2$ along the y-axis. The direction angle $\phi_i$, is defined as the angle between the vector $\overrightarrow{P_1P_2}$, and the x-axis. Duringcell rolling, $\phi_i$ varies sinusoidally with the translational displacement $y_i$, enablingestimation of the rotation period Y.

Once the rotational angles $\theta_i$ are estimated, we reconstruct the three-dimensional (3D) refractive-index (RI) distribution under the Rytov approximation. Let $u(r)$ and $u_0(r)$ denote the total and incident fields, respectively, and define the Rytov transform as

$$\psi(r) = \ln \frac{u(\boldsymbol{r})}{u_0(\boldsymbol{r})}.$$

For weak scattering (small RI contrast and negligible multiple scattering), higher-order terms in $\psi$ can be neglected, yielding a linear inverse problem. Accordingly, the 3D scattering potential can be expressed as:

$$f(r) = k_0^2 \left( \frac{n^2(r)}{n_0^2} - 1 \right),$$

where $n_0$ is the background RI and $k_0 = \frac{2\pi n_0}{\lambda_0}$ is the wavenumber in the background medium for vacuum wavelength $\lambda_0$. For each projection angle $\theta_i$, the two-dimensional (2D) Fourier transform of the Rytov field is mapped into 3D *k*-space according to the Fourier diffraction theorem, i.e. onto an Ewald-sphere surface of radius $k_0$ determined by the illumination/viewing geometry (under a small-angle approximation this surface can be approximated by a plane). Filling these surfaces across all $\theta_i$ produces a sampled estimate $\hat{f}(k)$; an inverse Fourier transform then yields $f(r)$.

$$n(r) = n_0 \sqrt{1 + \frac{f(r)}{k_0^2}},$$

Finally, the RI distribution is recovered from $f(r)$ as

$$n(r) \approx n_0 + \frac{n_0}{2k_0^2} f(r).$$

This Rytov-based pipeline offers a favorable trade-off between computational efficiency and robustness to moderate noise and model mismatch. Within the validity regime of single scattering, it yields reliable 3D cellular morphology suitable for downstream biophysical analysis.

**B. Fourier Shell Correlation analysis for resolution quantification**

To assess the fidelity of 3D RI reconstructions, we employed Fourier Shell Correlation (FSC) analysis[4,5]. FSC evaluates the similarity between two 3D volumes in the frequency domain, providing an objective measure of spatial resolution. Given two volumes $V_1$ and $V_2$ with Fourier transforms $F_1(k)$ and $F_2(k)$ where *k* denotes the spatial frequency vector, the FSC at spatial frequency $f = |k|$ is defined as:

$$FSC(f) = \frac{\sum_{k \epsilon S(f)} F_1(k)\, \overline{F_2(k)}}{\sqrt{\sum_{k \epsilon S(f)} |F_1(k)|^2 \sum_{k \epsilon S(f)} |F_2(k)|^2}},$$

where $S(f)$ denotes the shell of frequency vectors with magnitude *f*. The FSC curve plots correlation (0–1) against spatial frequency (in $\mu m^{-1}$), and typically decreases at higher frequencies due to reduced similarity between the two volumes at fine structural details.

The spatial resolution is defined as the inverse of the cutoff frequency at which the FSC

curve drops below a threshold:

$$Resolution = \frac{1}{f_{cutoff}}.$$

Two complementary evaluation strategies were adopted depending on data type[6]. Simulated data (with ground truth): the reconstructed volume was directly compared with the ground-truth volume, and the FSC=1/2 criterion was used to quantify resolution. Experimental data (without ground truth): since no reference volume is available for real experimental measurements, we cannot directly compare the reconstruction against ground truth. This limitation compels the use of alternative strategies for resolution assessment. Following the well-established practice in single-particle cryo-EM, we divided the full image sequence of each cell (or aggregate) into two statistically independent half-sets. Each subset was reconstructed into a separate 3D volume, and the resulting pair was compared using FSC. The FSC=1/7 criterion was then applied to determine the highest spatial frequency at which reproducible structural information can be reliably extracted.

## References


1. Villone, M. M. *et al.* Full-angle tomographic phase microscopy of flowing quasi-spherical cells. *Lab Chip* 18, 126–131 (2018).
2. Pirone, D. *et al.* Rolling angle recovery of flowing cells in holographic tomography exploiting the phase similarity. *Appl Opt* 60, A277–A284 (2020).
3. Li, Y. *et al.* Tomographic Flow Cytometry Based on Automatic Angle Recovery for Three-Dimensional Imaging of Carbon Nanoparticles in Bladder Cancer Cells. in *Digital Holography and Three-Dimensional Imaging* Th1A–6 (2024).
4. Ludtke, S. J., Baldwin, P. R. & Chiu, W. EMAN: semiautomated software for high-resolution single-particle reconstructions. *J Struct Biol* 128, 82–97 (1999).
5. Liao, H. Y. & Frank, J. Definition and estimation of resolution in single-particle reconstructions. *Structure* 18, 768–775 (2010).
6. Van Heel, M. & Schatz, M. Fourier shell correlation threshold criteria. *J Struct Biol* 151, 250–262 (2005).